

# LoFi: Scalable Local Image Reconstruction with Implicit Neural Representation

AmirEhsan Khorashadizadeh<sup>1</sup>, Tobías I. Liaudat<sup>2</sup>, Tianlin Liu<sup>3</sup>, Jason D. McEwen<sup>4</sup>, and Ivan Dokmanić<sup>1</sup>

**Abstract**—Neural fields or implicit neural representations (INRs) have attracted significant attention in machine learning and signal processing due to their efficient continuous representation of images and 3D volumes. In this work, we build on INRs and introduce a coordinate-based local processing framework for solving imaging inverse problems, termed LoFi (Local Field). Unlike conventional methods for image reconstruction, LoFi processes local information at each coordinate *separately* by multi-layer perceptrons (MLPs), recovering the object at that specific coordinate. Similar to INRs, LoFi can recover images at any continuous coordinate, enabling image reconstruction at multiple resolutions. With comparable or better performance than standard CNNs for image reconstruction, LoFi achieves excellent generalization to out-of-distribution data and memory usage almost independent of image resolution. Remarkably, training on  $1024 \times 1024$  images requires just 3GB of memory—over 20 times less than the memory typically needed by standard CNNs. Additionally, LoFi’s local design allows it to train on extremely small datasets with less than 10 samples, without overfitting or the need for regularization or early stopping. Finally, we use LoFi as a denoising prior in a plug-and-play framework for solving general inverse problems to benefit from its continuous image representation and strong generalization. Although trained on low-resolution images, LoFi can be used as a low-dimensional prior to solve inverse problems at any resolution. We validate our framework across a variety of imaging modalities, from low-dose computed tomography to radio interferometric imaging.

## I. INTRODUCTION

**I**MAGING inverse problems are ubiquitous in domains like medicine [Wang et al., 2008], material science [Holler et al., 2017], remote sensing [Blahut, 2004] and cosmology [Kaiser and Squires, 1993]. Deep learning has been, for a long time, the method of choice for solving inverse problems. In particular, convolutional neural networks (CNNs) like U-Net [Ronneberger et al., 2015] have shown remarkable performance across diverse tasks including computed tomography (CT) [Jin et al., 2017], magnetic resonance imaging (MRI) [Hyun et al., 2018], photoacoustic imaging [Davoudi et al., 2019] and inverse scattering [Wei and Chen, 2018]. The success of the U-Net is primarily attributed to its multiscale architecture with a large receptive field that extracts features from the input image at different scales [Liu et al., 2022].

Despite their strong performance on low-dimensional 2D imaging problems, deep learning architectures can become computationally expensive for high-dimensional images [Zhang et al., 2017a, Liang et al., 2021, Wang et al., 2021]. This inefficiency arises because current deep neural networks reconstruct the entire image simultaneously, necessitating substantial memory for back-propagation during training. Additionally, interpreting such complex architectures [Zhang et al.,

2021, Liang et al., 2021, Fabian et al., 2022] and analyzing their reconstructions can be challenging. Simplified neural architectures can enhance our understanding of reconstruction mechanisms, enabling the design of robust models with strong generalization [Aggarwal et al., 2018].

Recently, implicit neural representations (INRs) [Sitzmann et al., 2020, Atzmon and Lipman, 2020, Chabra et al., 2020] have emerged as a promising tool for representing continuous signals, images, and 3D volumes. Unlike most existing deep learning models that treat signals as discrete arrays, INRs map coordinates to signal values using a deep neural network, typically a multi-layer perceptron (MLP), resulting in a *continuous* signal representation. INRs have been widely applied to various tasks, including solving partial differential equations (PDEs) [Sitzmann et al., 2020, Vlašić et al., 2022, Khorashadizadeh et al., 2023a], 3D shape modeling [Chen and Zhang, 2019, Peng et al., 2020, Jiang et al., 2020], and image super-resolution [Chen et al., 2021b, Khorashadizadeh et al., 2023a]. One of the most well-known applications of INRs is 3D scene representation using neural radiance fields (NeRF) [Mildenhall et al., 2021].

INRs have several advantages over standard deep learning models. Rather than representing signals at a single resolution, INRs can conveniently interpolate signals in a continuous space. This capability is particularly interesting because we can conveniently adjust the required memory making INRs well-suited for high-dimensional 3D reconstructions [Dupont et al., 2021, 2022].

In this paper, we build on INRs and introduce a scalable coordinate-based local reconstruction pipeline for solving imaging inverse problems. In many tasks such as image denoising, super-resolution, and low-dose computed tomography (LDCT), the image intensity at a specific pixel is primarily influenced by the observed image in the pixel’s neighborhood. Our proposed model, termed LoFi (Local Field), recovers the image intensity at each pixel *separately*, using local information extracted from the input image around that pixel. This information is processed by a neural network (composed of MLP blocks) to determine the image intensity at the target pixel, enabling image reconstruction at any resolution or arbitrary continuous coordinate.

LoFi’s coordinate-based design brings several advantages. Similar to INRs, we can train LoFi on mini-batches of both objects and *pixels*, resulting in resolution-agnostic memory usage. As a result, LoFi can efficiently process high-resolution images with a tiny memory footprint. Notably, it requires just 3GB of memory to train on  $1024 \times 1024$  images. Furthermore, LoFi’s local design provides a strong inductive bias for image

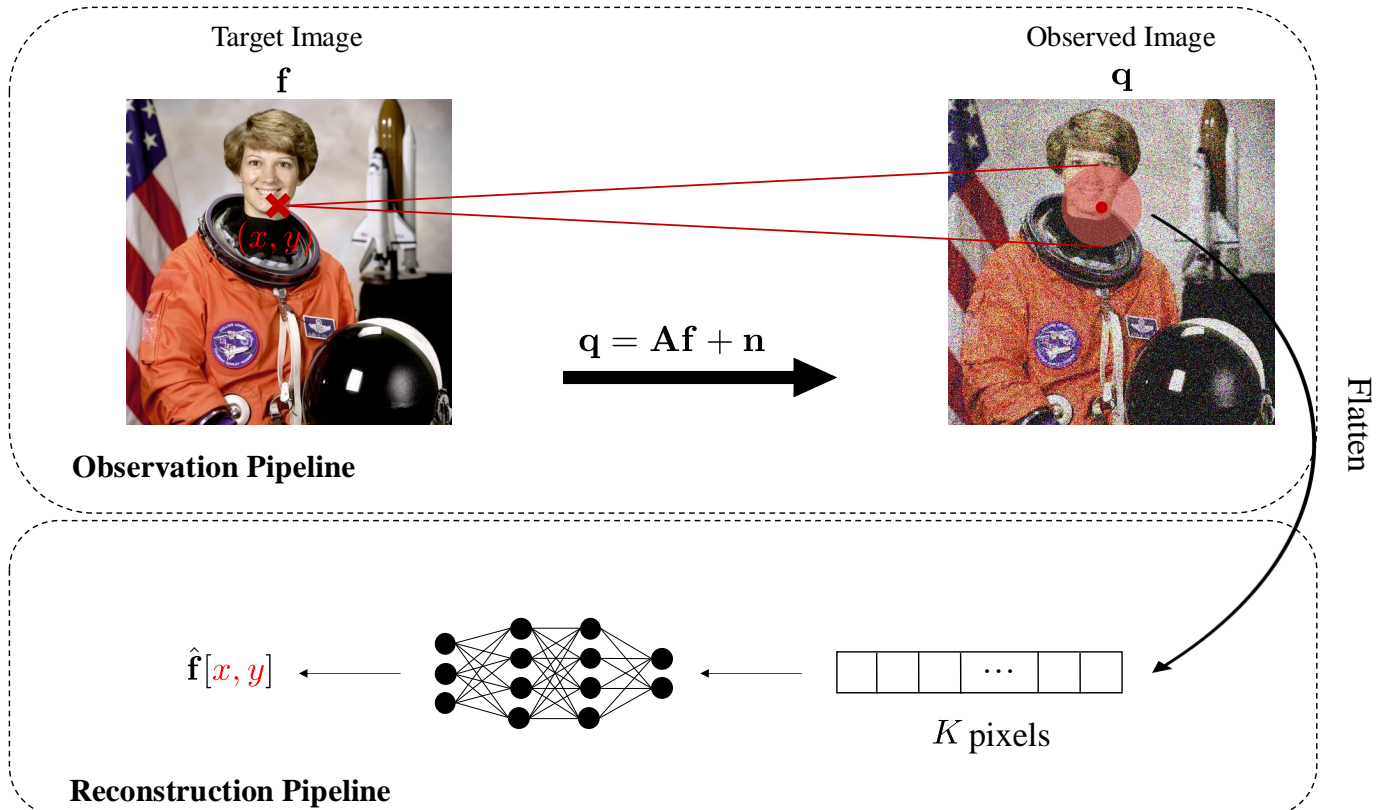


Fig. 1: LoFi; the neural network  $NN_\theta$ , typically composed of MLP modules, processes the local information extracted from the observed image around the given pixel  $(x, y)$ . LoFi’s inductive bias for image reconstruction brings strong generalization on OOD data, it requires less training data and uses small memory when training on high-resolution images.

reconstruction, as demonstrated in our experiments, where LoFi performs effectively on tiny datasets with very few samples, without overfitting or needing regularization and early stopping.

In addition, Deep learning models for image reconstruction like multiscale CNNs [Ronneberger et al., 2015, Zhang et al., 2021] and vision transformers (ViTs) [Liang et al., 2021, Wang et al., 2022, Fabian et al., 2022] often use sophisticated architectures that complicate downstream interpretations. Through our proposed coordinate-conditioned patch geometry, LoFi can learn the position of the relevant features in the input image for each pixel, providing insights for downstream image analysis and interpretation.

## II. BACKGROUND AND RELATED WORKS

The goal of an imaging inverse problem is to recover the image of interest  $f$  from noisy measurements  $q$  acquired via the potentially non-linear forward operator  $A$ ,

$$q = A(f) + n, \quad (1)$$

where  $n$  is noise. Inverse problems are often ill-posed, implying the existence of multiple plausible reconstructions for a given set of measurements. It is thus important to incorporate an image prior to enable stable and accurate reconstruction. While traditional hand-crafted priors such as total-variation (TV) [Osher et al., 2005] can yield good reconstructions, learning-based priors have brought about substantial improvements [Kothari et al., 2021, Jalal et al., 2021, Chung et al., 2022].

### A. Inverse problems with local operators

In many inverse problems, the forward operator is local; an image pixel primarily relates to its neighboring pixels in the observed image. Here the assumption is that the observed data is shaped like an image with the same coordinate system as the target. A local forward operator suggests an opportunity to design efficient deep-learning architectures. In the following, we discuss three inverse problems characterized by this localization property.

#### Image denoising:

The most straightforward inverse problem is image denoising, where the forward operator  $A$  in (1) is the identity matrix; each pixel in the clean image is solely connected to the corresponding pixel in the noisy image, assuming independent noise (between pixels) and natural images. Despite this simplicity, the presence of noise prompts the incorporation of ‘contextual’ information from neighboring noisy pixels. In principle, the required local neighborhood size depends on the noise level and the prior distribution; stronger noises often necessitate larger receptive fields for natural images [Levin and Nadler, 2011].

#### Low-dose Computed Tomography:

Low-dose computed tomography (LDCT) is a medical imaging technique that reduces radiation exposure to patients during a CT scan by lowering the X-ray beam intensity. Traditional CT imaging uses X-rays to capture cross-sectional images of the body, but these scans can result in significant radiation doses,

potentially increasing the risk of long-term side effects like cancer [Brenner and Hall, 2007]. LDCT mitigates these risks by significantly lowering the X-ray dose without compromising diagnostic quality, making it a safer imaging process.

CT image reconstruction can be viewed as an inverse problem,

$$\mathbf{y} = \mathcal{R}(\mathbf{x}) + \mathbf{n}, \quad (2)$$

where the forward operator  $\mathcal{R}$  is the radon transform applied in angles  $\{\alpha_i\}_{i=1}^r$  and  $\mathbf{n}$  is the additive noise. In LDCT, the projections  $\mathbf{y}$  are collected from sufficient angles  $r$  but using low-intensity beams resulting in noisy projections. The standard approach for CT image reconstruction is filtered backprojection (FBP),

$$\mathbf{x}_{\text{FBP}} = \mathcal{R}_{\text{FBP}}(\mathbf{y}). \quad (3)$$

In an ideal scenario where we have an infinite number of noise-free projections, FBP is the exact inverse, namely,  $\mathbf{x}_{\text{FBP}} = \mathbf{x}$ . In LDCT, we have a sufficient number of noisy projections  $N$ , the image reconstruction from FBP can be seen as a denoising problem,

$$\mathbf{x}_{\text{FBP}} \approx \mathbf{x} + \mathcal{R}_{\text{FBP}}(\mathbf{n}). \quad (4)$$

The image reconstruction from FBP can be seen as an inverse problem with a local forward operator for LDCT.

#### Dark matter mapping in cosmology:

As another example, we consider dark matter mapping [Kaiser and Squires, 1993] in cosmology which is important for understanding the nature of dark matter in the Universe through the use of weak gravitational lensing [Mandelbaum, 2018]. We will study the convergence that traces the projected mass distribution of dark matter in the Universe. The goal is to estimate the convergence field  $\kappa$ , the target image, from a related observable, the shear field  $\gamma$ . The convergence is associated with the magnification of observed galaxies, while the shear corresponds to the image’s stretching due to ellipticity changes. The two fields are related as

$$\gamma = \mathbf{A}\kappa + \mathbf{n}, \quad (5)$$

where  $\mathbf{n}$  is the shear field noise, and the forward operator  $\mathbf{A}$  is a convolutional filter (a Fourier multiplier) with the 2D Fourier transform given by<sup>1</sup>,

$$\mathbf{D}_{k_x, k_y} = \frac{k_x^2 - k_y^2 + 2ik_x k_y}{k_x^2 + k_y^2}, \quad \text{for } k_x^2 + k_y^2 \neq 0. \quad (6)$$

A simple approach to recover the convergence field  $\kappa$  from the shear field  $\gamma$  is the Kaiser-Squires (KS) method [Kaiser and Squires, 1993], the current standard in cosmology. The method consists of directly applying  $\mathbf{A}^{-1}$ , the inverse of the forward operator, to the shear field, with a subsequent Gaussian smoothing with an ad hoc setting of the smoothing scale. We consider the naive KS inversion, without the Gaussian smoothing step, as follows,

$$\kappa_{\text{KS}} = \mathbf{A}^{-1}\mathbf{A}\gamma = \kappa + \mathbf{A}^{-1}\mathbf{A}\mathbf{n} = \kappa + \tilde{\mathbf{n}}, \quad (7)$$

where  $\tilde{\mathbf{n}} = \mathbf{A}^{-1}\mathbf{A}\mathbf{n}$ . The recovery of the convergence field from the naive inverted KS image is thus an inverse problem with a *local* forward operator.

<sup>1</sup>This is known as the weak lensing planar forward model.

## B. Deep learning for image reconstruction

Over the last decade, various deep learning approaches have achieved state-of-the-art (SOTA) performance in image reconstruction. Some early approaches segmented the image into patches and employed an MLP to denoise each patch individually [Burger et al., 2012]. However, the optimal patch size for high-quality reconstructions depends on the noise level and data distribution. Zhang et al. [Zhang et al., 2017a] introduced DnCNN, an image-to-image CNN designed for image denoising where the network depth is adjusted based on the required receptive field size suggested by traditional methods [Zoran and Weiss, 2011]. To expand CNN’s receptive field and use more contextual information, they used dilated convolutions [Zhang et al., 2017b]. Concurrently, the U-Net [Ronneberger et al., 2015] has been the backbone model for SOTA image reconstruction architectures [Liu et al., 2018, Park et al., 2019, Jia et al., 2021, Liu et al., 2022], in particular, the DRU-Net [Zhang et al., 2021] achieved remarkable performance by integrating residual blocks [He et al., 2016] into the U-Net architecture. Despite their success, these CNNs lack a systematic procedure for automatic adjustment of the required receptive field size; a tiny receptive field hinders the model performance leading to sub-optimal reconstructions while an excessively large receptive field can result in overfitting the large-scale features and poor generalization.

More recently, vision transformers (ViTs) [Dosovitskiy et al., 2020] have achieved comparable or even better performance than CNNs for various image reconstruction tasks [Chen et al., 2021a, Liang et al., 2021, Wang et al., 2022, Mansour et al., 2022]. The core concept of ViTs is to divide the input image into non-overlapping patches, transform each patch into an embedding using a learned linear projection, and then process the resulting tokens through a series of stacked self-attention layers and MLP blocks. The advantage of ViTs over CNNs is attributed to their ability to capture long-range dependencies in the images through the self-attention mechanism [Zamir et al., 2022]. A major challenge for ViTs in image reconstruction is the quadratic computational complexity of global self-attention relative to the input image size [Wang et al., 2021]. Some approaches have addressed this by designing hierarchical transformers [Heo et al., 2021, Wang et al., 2021]. The authors of [Fabian et al., 2022] use convolutional blocks to reduce the spatial dimensions followed by self-attention blocks applied in different scales. Despite the marginally better reconstructions compared to CNNs for inverse problems with non-local forward operators like magnetic resonance imaging (MRI), they show comparable performance with CNNs for local problems like image denoising [Fabian et al., 2022]. Moreover, unlike CNNs, ViTs do not benefit from the appropriate inductive bias for image generation, necessitating huge datasets for training [Dosovitskiy et al., 2020, Mansour et al., 2022].

In this paper, we demonstrate that for inverse problems with local forward operators, such as those discussed in Section II-A, it is not necessary to process large-scale features using multiscale CNNs or ViTs. Instead, our proposed architecture efficiently captures local features, resulting in strong generalization while significantly reducing computational costs

and memory requirements, well-suited for high-dimensional image reconstruction.

### C. Patch-based image reconstruction

While traditional methods for image reconstruction often process small patches extracted from the input image [Buades et al., 2005, Dabov et al., 2007], deep learning models with patch-based design have recently gained considerable attention. ViTs [Dosovitskiy et al., 2020] and MLP-mixers [Tolstikhin et al., 2021] are a well-known family of patch-based models whose strong performance is often attributed to patch-based design [Trockman and Kolter, 2022]. Deep generative models trained on small patches have been used for high dimensional image generation [Ding et al., 2024] and more efficient training on datasets with significantly fewer images [Wang et al., 2024]. Patch priors [Gilton et al., 2019, Altekrüger et al., 2022, Hertrich et al., 2022] as efficient alternatives to image priors have been used for image reconstruction which allows training on small datasets with few images well-suited for scientific tasks where we have access to a limited number of ground truth images.

### III. LOFI: A LOCAL FIELD PROCESSOR

Our objective is to reconstruct the target image  $\mathbf{f} \in \mathbb{R}^{N \times N \times C}$  from the observed image  $\mathbf{q} \in \mathbb{R}^{M \times M \times C}$ , as described in the forward equation (1), where  $C$  is the channel dimension,  $N$  and  $M$  denote the resolution of the target and observed images. The resolutions of  $\mathbf{f}$  and  $\mathbf{q}$  may be different but we assume that they share the same coordinate system and semantics; thus  $\mathbf{f}[x, y]$  and  $\mathbf{q}[x, y]$  refer to the same continuous location in both images. Example problems where this is meaningful are denoising and deblurring. More generally, for many linear inverse problems, including computed tomography, it will hold after applying the adjoint of the forward operator as shown in (4).

We then consider a local forward operator  $\mathbf{A}$  where the intensity  $\mathbf{f}[x, y]$  at pixel  $(x, y) \in \mathbb{R}^2$  relates only to a small neighborhood of  $(x, y)$  in  $\mathbf{q}$ . Based on this locality hypothesis, we design a coordinate-based neural network inspired by implicit neural representation.

To recover the image at the target pixel  $(x, y)$  *individually*, we extract local information around  $(x, y)$  from the observed image  $\mathbf{q}$  containing  $K$  pixels. We denote the (flattened) extracted information by  $\mathbf{p}_{x,y} \in \mathbb{R}^{K \times C}$ . As illustrated in Figure 1, we process  $\mathbf{p}_{x,y}$  using a neural network  $\text{NN}_\theta : \mathbb{R}^{K \times C} \rightarrow \mathbb{R}^C$  with parameters  $\theta$  to approximate the image intensity  $\mathbf{f}[x, y]$ ,

$$\hat{\mathbf{f}}[x, y] = \text{NN}_\theta(\mathbf{p}_{x,y}). \quad (8)$$

This coordinate-based image representation enables image recovery at any continuous coordinate with small memory. We call our framework LoFi (Local Field). As we typically use a small neighborhood size  $K$ , we can parametrize  $\text{NN}_\theta$  using an MLP. It is worth noting that a similar framework is used in [Khorashadizadeh et al., 2023a] for continuous image super-resolution using CNNs. In the following sections, we provide further details regarding the LoFi architecture and introduce the pre-processing filter, patch geometry, and training strategy.

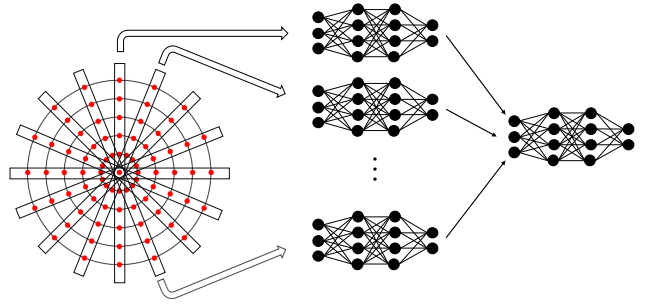


Fig. 2: MultiMLP architecture; the input information is split into smaller chunks each processed with a separate MLP, the extracted information is then mixed by another MLP.

#### A. MultiMLPs for large neighborhoods

One important factor in LoFi architecture is the neighborhood dimension  $K$ ; larger  $K$  can provide more detailed information to improve reconstructions. However, by increasing  $K$ , the size of MLP quadratically scales resulting in a bulky network and slow training. To address this issue, we propose MultiMLP, an alternative architecture to the current MLP to handle large neighborhoods. Inspired by vision transformers [Dosovitskiy et al., 2020], we split the extracted neighboring pixels (here over a circular geometry) into smaller chunks, each processed by a separate MLP as shown in Figure 2. Their outputs are then mixed by another MLP.

#### B. Patch geometry and equivariance

A straightforward method to extract the neighboring pixels is to directly select the pixels adjacent to the target pixel  $(x, y)$ . This however has several drawbacks: it requires a manual selection of the neighborhood size, akin to traditional methods, which is hard to estimate; it only permits image evaluation at on-grid pixels resulting in a single-resolution image reconstruction.

1) *Differentiable patch extraction*: While we can use the standard square patch to extract the local information, it does not provide a differentiable operator from the input coordinate to the pixel intensity. To enable image reconstruction at arbitrary continuous coordinates, we extract the local information  $\mathbf{p}_{x,y}$  using bicubic interpolation, providing a continuous differentiable operator.

2) *Learnable patch geometry*: The differentiable patch extraction suggested above also brings important flexibility; it allows us to learn the patch geometry centered around the target coordinate  $(x, y)$  by first defining a set of *learnable* coordinate offsets,

$$\Delta I = [(x_n^\Delta, y_{n'}^\Delta)]_{n,n'=1}^K. \quad (9)$$

By learning the optimal coordinate offsets  $\Delta I$  we can also control the scale and shape of the patch receptive field. We then extract the patch by evaluating  $\mathbf{q}$  at coordinates  $I_{(x,y)} = (x, y) + \Delta I$  to get

$$\mathbf{p}_{x,y} = \mathbf{q}[I_{(x,y)}]. \quad (10)$$

We emphasize that the coordinates  $I_{(x,y)}$  need not be aligned with the pixel grid as we use differentiable bicubic interpolation

to enable off-the-grid evaluation. Unlike most other work using square patches, we initialize  $\Delta I$  to a circular geometry; this results in better rotation invariance as discussed in Section S-II-B in the supplementary materials.

### C. Coordinate-conditioned patch geometry

While the learnable patch geometry introduced in (9) can provide additional flexibility to the network, the learned patch geometry is fixed for all the pixels in the image. In practice, the location of the relevant information changes for different pixels. To enable coordinate-conditioned patch geometry (CCPG), we use another neural network (typically a simple MLP)  $\text{CCPG}_\psi : \mathbb{R}^{K \times C} \rightarrow \mathbb{R}^{2K}$  which takes a local patch around pixel  $(x, y)$  and estimates the position of the coordinates inside the patch as follows,

$$\Delta I_{\text{CCPG}}(x, y) = \text{CCPG}_\psi(p_{x,y}). \quad (11)$$

We then evaluate  $\mathbf{q}$  at  $(x, y) + \Delta I_{\text{CCPG}}(x, y)$ . The learned patch geometry  $\Delta I_{\text{CCPG}}(x, y)$  can localize the position of the relevant information for image recovery at pixel  $(x, y)$  for corrupted image  $\mathbf{q}$ . It is worth noting that a similar strategy has been developed by [Dai et al., 2017] for object detection using CNNs.

Now we can improve the localization performance by repeating this process  $T$  times,

$$\Delta I_{\text{CCPG}}^{(i)}(x, y) = \text{CCPG}_\psi^{(i)}(p_{x,y}^{(i-1)}) \quad (12)$$

$$p_{x,y}^{(i)} = \mathbf{q}[(x, y) + \Delta I_{\text{CCPG}}^{(i)}(x, y)] \quad (13)$$

where in each iteration  $1 \leq i \leq T$ , we feed noisy image  $\mathbf{q}$  evaluated at the estimated patch position in the previous step  $p_{x,y}^{(i-1)}$  to a separate neural network  $\text{CCPG}_\psi^{(i)}$ . As we will show in our experiments in Section V-B, the learned patch geometry indeed improves over iterations.

### D. Noise suppression filter

The observed image  $\mathbf{q}$  is often corrupted with significant noise making the inversion challenging for the  $\text{NN}_\theta$  in (8). To address this, we apply pre-processing filters  $\mathbf{h} \in \mathbb{R}^{s \times s \times L}$  to the observed image before patch extraction,

$$\tilde{\mathbf{q}} = \mathbf{q} \star \mathbf{h}, \quad (14)$$

where  $\star$  denotes the convolution operator,  $s$  is the filter size and  $L$  is the number of filters. This process is reminiscent of filtering techniques commonly used in computed tomography imaging [Diwakar and Kumar, 2018]. We can also concatenate the filtered and noisy images along the channel dimension.

To avoid manual adjustment of the receptive field, we apply the filter in the frequency domain,

$$\tilde{\mathbf{q}} = \mathbf{F}^{-1} \mathbf{H} \mathbf{F} \mathbf{q}, \quad (15)$$

where  $\mathbf{F}$  and  $\mathbf{F}^{-1}$  are the forward and inverse 2D Fourier transforms, and the filter  $\mathbf{H}$  is treated as a learnable parameter derived from the data. The filter  $\mathbf{H}$  can have large support in image space, capturing global information, in contrast to the local convolutional operator in (14). This large filter support can allow the  $\text{NN}_\theta$  to overfit global features and compromise

model generalization. To mitigate this issue, we initialize the filter  $\mathbf{H}$  with an all-one Fourier representation, which corresponds to the smallest support in pixel space. During training, the filter expands its support based on the image resolution, noise level, and data distribution while keeping the filter support small. To further control support size, we could add a regularization penalty based on the filter support but in subsequent experiments presented in Section S-II-C in the supplementary materials, we noticed that the learned filter has small support even without any regularization.

### E. Resolution-agnostic memory usage in training

For simplicity, we write the entire LoFi pipeline as  $\hat{\mathbf{f}}(\mathbf{x}) = \text{LoFi}_\phi(\mathbf{x}, \mathbf{q})$  where  $\mathbf{x} = (x, y)$  is the target pixel. The model approximates the image intensity  $\hat{\mathbf{f}}(\mathbf{x})$  from the observed image  $\mathbf{q}$ . We denote all the trainable parameters of LoFi by  $\phi$ . This includes  $\theta$ , pre-processing filter parameters  $\mathbf{h}$ , and CCPG weights  $\psi$ . We consider a set of training data  $\{(\mathbf{q}_i, \mathbf{f}_i)\}_{i=1}^D$  from observed and target images. We optimize the LoFi parameters  $\phi$  using a gradient-based optimizer to solve,

$$\phi^* = \underset{\phi}{\text{argmin}} \sum_{i=1}^D \sum_{j=1}^{N^2} |\mathbf{f}_i(\mathbf{x}_j) - \text{LoFi}_\phi(\mathbf{x}_j, \mathbf{q}_i)|. \quad (16)$$

At inference time, we can recover the image at any target pixel  $\mathbf{x}$  from the observed image  $\mathbf{q}_{\text{test}}$  as  $\hat{\mathbf{f}}_{\text{test}}(\mathbf{x}) = \text{LoFi}_{\phi^*}(\mathbf{x}, \mathbf{q}_{\text{test}})$ . From (16), it is clear that LoFi can be trained on mini-batches of both objects *and* pixels, leading to nearly constant memory usage during training and inference. This flexibility also allows us to train LoFi on datasets with images in various resolutions.

## IV. FURTHER APPLICATIONS

In this section, we discuss further applications of the proposed local processing framework.

### A. Learning the imaging geometry

Many seemingly complex image-to-image transforms, like those involving translations and rotations, alter image content using simpler coordinate transformations. For example, transposing a 2D image causes significant pixel differences in high-dimensional space; but this transformation relies on a simple, low-dimensional coordinate swap. When CNNs are fitted on image-to-image tasks, they are directly trained to model the changes in pixel values and, therefore, tend to overlook the coordinate transformations that underlie the pixel value changes. This is particularly problematic for large-scale changes in the coordinate system as the CNN should have a large receptive field to capture these geometric changes. This limitation has been explored by existing works to build deep neural networks that can model the changes in the coordinate system as well as the image content. For example, the authors of [Kothari et al., 2020] separately model changes of the coordinate system and the image content using CNNs.

Although LoFi can only learn the local changes in the *image content*, its coordinate-based design allows us to easily equip it to learn the changes in the coordinate system as well. To this end, we use an  $\text{INR}_\eta$  with parameters  $\eta$ , that takes the given

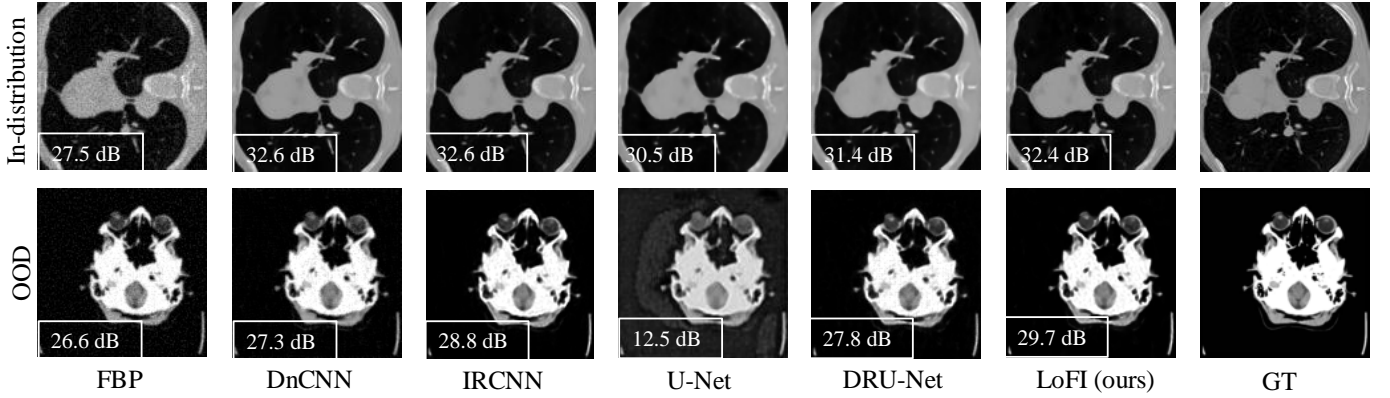


Fig. 3: Performance comparison on LDCT (30dB noise) in resolution  $128 \times 128$ .

coordinate  $\mathbf{x}$  and returns the new coordinate  $\tilde{\mathbf{x}}$ . This INR is then followed by LoFi to sample from the local neighborhood around  $\tilde{\mathbf{x}}$  from the input image  $\mathbf{q}$  as follows,

$$\tilde{\mathbf{x}} = \text{INR}_{\eta}(\mathbf{x}), \quad (17)$$

$$\hat{\mathbf{f}}(\mathbf{x}) = \text{LoFi}_{\phi}(\tilde{\mathbf{x}}, \mathbf{q}). \quad (18)$$

We train the above architecture end-to-end where the task of INR is to learn the changes in the coordinate system, while LoFi learns the changes in the image content from the corrected coordinate system. We call this new architecture INR-LoFi and compare its performance with CNNs for a toy experiment in Section V-C.

### B. Low-resolution priors for high-resolution unsupervised image reconstruction

As shown in Section III-E, the proposed LoFi is a *supervised* learning framework that provides fast image recovery from observations. However, supervised learning methods necessitate paired training data comprising measurements and corresponding target images which is hard to obtain in many real scientific problems [Jin et al., 2017, McCann et al., 2017, Liu et al., 2022, Wei and Chen, 2018, Khorashadizadeh et al., 2023c]. Additionally, the related models require re-training even for small changes in the forward model.

To address this issue, unsupervised methods learn a data-driven prior from target images. Deep generative models have been extensively used for solving imaging inverse problems where a pre-trained image generator is used as the prior [Bora et al., 2017, Kothari et al., 2021, Asim et al., 2020, Kawar et al., 2022, Khorashadizadeh et al., 2023b, Liu et al., 2023]. However, training deep generative models often requires large-scale datasets and substantial computational resources [Kingma and Dhariwal, 2018, Ho et al., 2020].

An alternative is to use a Gaussian denoiser as a prior in a plug-and-play (PnP) framework [Venkatakrishnan et al., 2013, Chan et al., 2016, Romano et al., 2017]. PnP algorithms achieved SOTA performance across a variety of image reconstruction tasks including image super-resolution and deblurring [Dong et al., 2018, Zhang et al., 2021], computed tomography (CT) [Wei et al., 2022] and magnetic resonance imaging (MRI) [Ahmad et al., 2020, Wei et al., 2020]; see

also the recent review [Kamilov et al., 2023]. Since PnP algorithms decouple the likelihood from the image prior they enable the use of pre-trained denoisers. Compared to generative priors they are often cheaper in both training and inference. Recently, the authors of [Zhu et al., 2023] leveraged diffusion models [Ho et al., 2020, Dhariwal and Nichol, 2021] as a pre-trained denoiser in PnP framework and achieved excellent performance for various image restoration tasks. We provide a brief overview of the PnP-ADMM framework in Section S-I-E of the supplementary material.

In this section, we use a pre-trained LoFi denoiser as a prior in the plug-and-play (PnP) framework to benefit from its continuous image representation for solving inverse problems; this integration allows us to use a LoFi denoiser trained on *low-resolution* images for solving inverse problems at *any* higher resolution.

We employ a pre-trained LoFi denoiser in PnP-ADMM and call this framework LoFi-ADMM described in Algorithm 1. Remarkably, while we train LoFi denoiser on low-resolution images, LoFi-ADMM can conveniently run at any arbitrary higher resolutions thanks to the continuous image representation of LoFi.

---

#### Algorithm 1: LoFi-ADMM

---

**Input:**  $\mathbf{q}, \mathbf{A}, \phi^*$

**Parameter:**  $\alpha$

$\mathbf{f} = 0, \mathbf{u} = 0, \mathbf{v} = 0;$

**for**  $k = 0$  **to**  $K - 1$  **do**

$\mathbf{f}_k \leftarrow h(\mathbf{v}_{k-1} - \mathbf{u}_{k-1}; \alpha);$

$\mathbf{v}_k(\mathbf{x}) \leftarrow \text{LoFi}_{\phi^*}(\mathbf{x}, \mathbf{f}_k - \mathbf{u}_{k-1}), \quad \forall \mathbf{x} \in \mathbf{v}_k;$

$\mathbf{u}_k \leftarrow \mathbf{u}_{k-1} + (\mathbf{f}_k - \mathbf{v}_k);$

**end**

---

## V. EXPERIMENTS

We run extensive experiments to evaluate the performance of LoFi from different aspects. In Section V-A, we compare LoFi with successful CNNs for several image reconstruction tasks. In Section V-B, we use our proposed method in Section III-C for analysis and interpretation of the reconstructed image. In Section V-C, we showcase the success of INR-LoFi and the

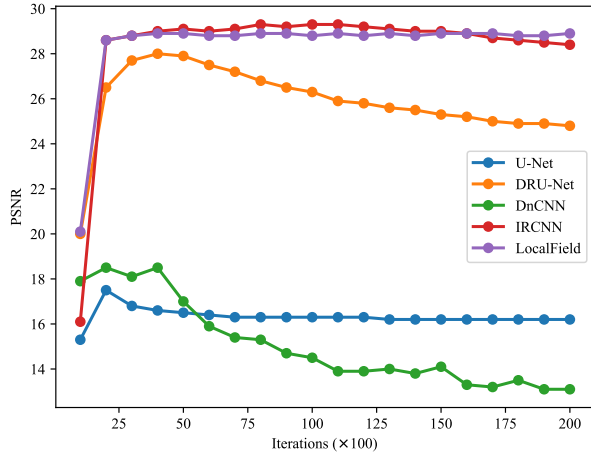


Fig. 4: Comparative analysis for image denoising in resolution  $512 \times 512$  where different models are trained on a tiny dataset with 9 training samples. The PSNR of the reconstructed test samples is demonstrated per iterations during training. CNNs in particular multiscale versions show severe overfitting while LoFi shows a robust convergence and significantly outperforms CNNs thanks to its locality design.

failure of CNNs on a simple toy experiment where we have changes in the coordinate system. We compare LoFi with CNNs in terms of memory usage and training time in Section V-D. In Section V-E, we apply our unsupervised framework LoFi-ADMM to two inverse problems, image in-painting and radio interferometry in cosmology.

#### A. Scalable image reconstruction with LoFi

We assess the performance of LoFi on inverse problems with local forward operators including low-dose computed tomography (LDCT), image denoising, and dark matter mapping in cosmology. As baselines, we consider standard CNNs including two single-scale models DnCNN [Zhang et al., 2017a] and IRCNN [Zhang et al., 2017b] and two multiscale models, U-Net [Ronneberger et al., 2015] and DRU-Net [Zhang et al., 2021]. We assess the reconstruction quality with peak signal-to-noise ratio (PSNR) and Structural Similarity Index (SSIM) [Wang et al., 2004]. Further details regarding the LoFi architecture and training details are available in Section S-I in the supplementary materials.

##### Low-dose computed tomography:

We simulate parallel-beam low-dose CT with  $r = 180$  projections uniformly distributed around the object. The measured projections are contaminated with 30dB Gaussian noise. We use 1000 training samples of chest images from the LoDoPaB-CT dataset [Leuschner et al., 2021] in resolution  $128 \times 128$ . The model performance is assessed on 100 in-distribution test samples of chest images and we use 16 brain samples [Hssayeni et al., 2020] to evaluate model generalization on out-of-distribution (OOD) data.

The upper row of Figure 3 illustrates the performance of different models on in-distribution chest images. Interestingly, LoFi can achieve comparable performance with standard CNNs

TABLE I: Model comparison on the reconstruction quality for LDCT (30dB SNR) averaged on 100 in-distribution chest and 16 OOD brain samples.

	In-dist (chest)		OOD (brain)	
	PSNR	SSIM	PSNR	SSIM
FBP	26.0	0.55	26.0	0.61
DnCNN [Zhang et al., 2017a]	34.2	0.90	27.6	0.82
IRCNN [Zhang et al., 2017b]	<b>34.5</b>	<b>0.91</b>	29.8	0.93
U-Net [Ronneberger et al., 2015]	33.0	0.90	13.9	0.81
DRU-Net [Zhang et al., 2021]	33.8	0.90	29.0	0.90
LoFi (ours)	33.9	0.90	<b>30.6</b>	<b>0.94</b>

by using only MLP modules. The lower row demonstrates the model performance on out-of-distribution (OOD) brain samples. LoFi significantly outperforms CNNs, indicating the strong generalization achieved by the locality of the architecture.

##### Image denoising:

In this experiment, we consider image denoising where we use a very small dataset of only 10 images at a resolution  $512 \times 512$  —9 images for training and 1 for testing, shown in Figure S1 in the supplementary materials. The images are normalized to a range between 0 and 1, and zero-mean Gaussian noise with  $\sigma = 0.15$  is added. We compare LoFi with various CNNs with a comparable number of weights (3M). Figure 4 presents the PSNR of the reconstructed test image across training iterations for each model. While strong CNNs such as DRU-Net, U-Net, and DnCNN initially perform well, they quickly overfit the training data, leading to a sharp drop in test image performance. IRCNN demonstrates improved generalization but also begins to overfit after 10000 iterations. Remarkably, LoFi shows strong generalization due to its locality design, avoiding overfitting even on this small dataset. This experiment clearly shows that we can conveniently train LoFi on a tiny dataset without being concerned about overfitting and needing early stopping or other regularization techniques. Final reconstructions after 20000 iterations are illustrated in Figure 5.

##### Dark matter mapping:

As shown in (7), the dark matter mapping problem can be interpreted as a denoising problem characterized by a local forward operator. We apply LoFi on the naive KS inversion  $\kappa_{KS}$  to recover the convergence field  $\kappa$ . For additional details regarding the experimental setup, please refer to Section S-I-C in the supplementary materials.

In Figure 6, the reconstructed convergence fields from the KS image are presented for various models at resolution  $128 \times 128$ . The performance parity between LoFi and CNNs indicates the validity of the locality property derived from (7).

#### B. Reconstruction analysis and interpretation

As discussed in Section III-C, LoFi adaptively estimates patch geometry for each pixel based on local information. Figure 7 illustrates the learned patch geometry across different pixels for the image denoising task, where the estimated positions of relevant features align with intuitive expectations. This ability to pinpoint features contributing to each pixel’s estimation can be valuable for more insightful analysis and interpretation. Additionally, the figure shows that more iterations

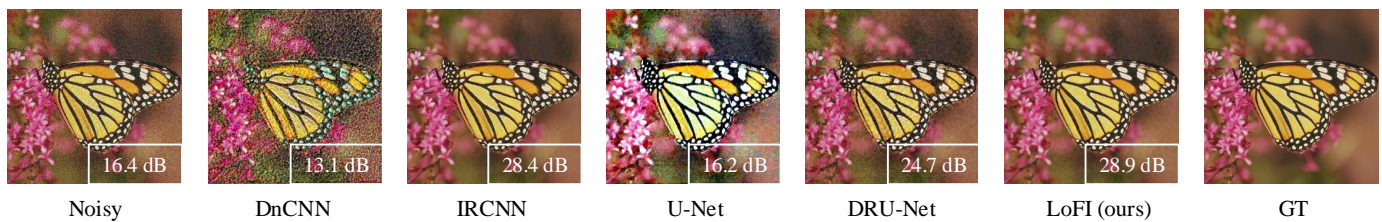


Fig. 5: Performance comparison on image denoising where different models are trained for 20000 iterations on a tiny training set with 9 images shown in Figure S1.

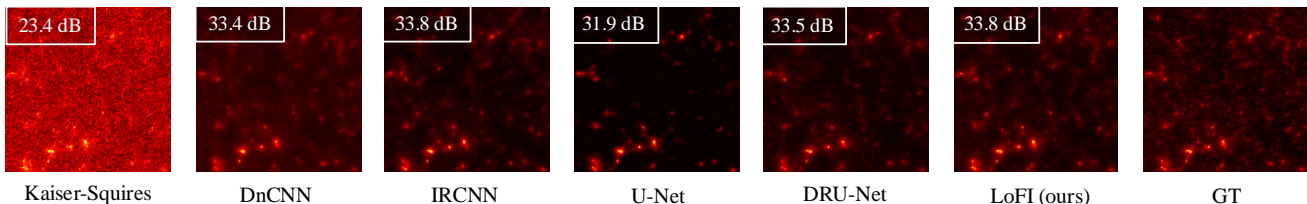


Fig. 6: Performance comparison on reconstructed convergence fields for dark matter mapping in resolution  $128 \times 128$ .

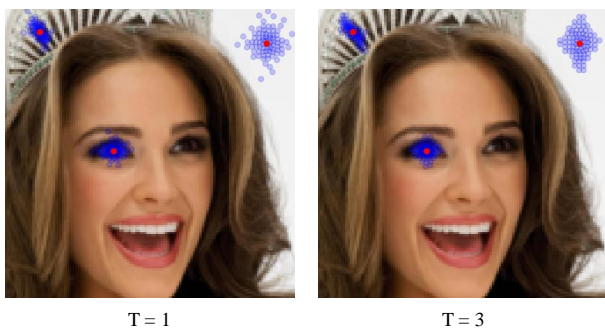


Fig. 7: The learned patch geometry for different pixels. As expected, larger  $T$  results in more accurate localization of the relevant information.

(larger values of  $T$ ) yield more precise localization of relevant information, enhancing the effectiveness of feature selection.

### C. Learning the imaging geometry with INR-LoFi

In this section, we study the performance of different models on a toy experiment where we have changes in the coordinate system. We consider recovering an image from its transpose; a simple task where we only have changes in the coordinate system while the image content remains unchanged. We train LoFi and CNNs on 29900 training samples from CelebA-HQ [Karras et al., 2017] dataset. Figure 8 showcases the performance of different models on both in-distribution (CelebA-HQ test samples) and OOD data (LSUN-bedroom [Yu et al., 2015]). Despite the simplicity of the task and access to a large-scale dataset, CNNs show poor performance as they can only learn the changes in the image content while neglecting the changes in the coordinate system. Unlike CNNs, our proposed INR-LoFi can conveniently learn these changes in the coordinate system resulting in significantly better reconstructions.

TABLE II: Model comparison for memory usage and training time on one epoch.

	Params	$128 \times 128$	$256 \times 256$	$512 \times 512$	$1024 \times 1024$
DnCNN [Zhang et al., 2017a]	3M	23GB / 200s	78GB / 1680s	> 80GB	> 80GB
IRCNN [Zhang et al., 2017b]	3M	16GB / 120s	55GB / 500s	> 80GB	> 80GB
U-Net [Ronneberger et al., 2015]	8M	6GB / 40s	16GB / 100s	60GB / 380s	> 80GB
DRU-Net [Zhang et al., 2021]	8M	7GB / 60s	22GB / 220s	79GB / 800s	> 80GB
LoFi (with filter; ours)	4M	3GB / 80s	3GB / 100s	5GB / 140s	15GB / 300s
LoFi (no filter; ours)	3M	2GB / 60s	2GB / 80s	2GB / 120s	3GB / 260s

### D. Computational efficiency

As discussed in Section III-E, LoFi can operate on machines with extremely small GPUs by reducing the pixel batch size in both training and inference. We train all models with the same object batch size 64 on a dataset with 30000 training samples from CelebA-HQ dataset. Table II presents a comparative analysis of memory usage and training time (per epoch) across different models and image resolutions. This analysis highlights that, while CNN memory requirements scale with image resolution, LoFi’s memory usage remains nearly constant, requiring only 3GB for resolutions above  $512 \times 512$ —over 20 times less than the typical memory needed for CNNs.

To address the significant memory demands of CNNs for large images, one common workaround is to train on smaller image patches. However, this approach is suboptimal due to the manual selection of patch size and the need to mitigate blocking artifacts at inference. Moreover, this patch-based training strategy is only effective for local tasks, such as image denoising, where the relevant information can be found within the corresponding input patch. For non-local tasks, like those discussed in Section V-C, this approach breaks down because the required information often lies outside the corresponding patch, making accurate reconstruction almost impossible.

### E. Low-resolution priors for high-resolution image reconstruction with LoFi-ADMM

As discussed in Section IV-B, LoFi can be used as a low-dimensional prior for processing the measurements acquired



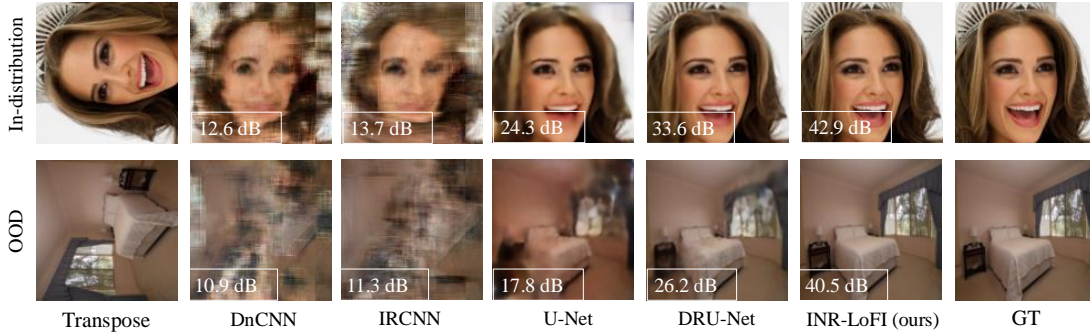


Fig. 8: Performance comparison on toy experiment of recovering an image from its transpose.

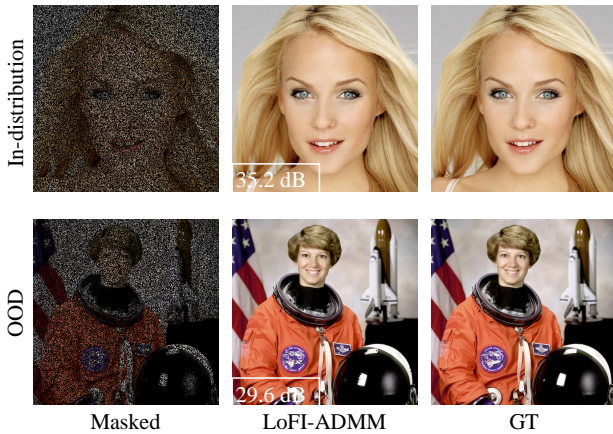


Fig. 9: LoFi-ADMM performance on image in-painting ( $p = 30\%$ ) for in-distribution and OOD data in resolution  $512 \times 512$  when LoFi denoiser is trained on CelebA-HQ samples in low resolution  $128 \times 128$ .

at higher resolutions. To this end, we train LoFi denoiser on low-resolution images and use it as a prior in LoFi-ADMM for solving two inverse problems at higher resolutions; image in-painting and radio interferometric imaging.

**Image in-painting.** We train LoFi denoiser on 29900 samples from the CelebA-HQ [Karras et al., 2017] in low resolution  $128 \times 128$  where we consider zero-mean Gaussian noise  $\mathbf{n}$  with  $\sigma = 0.15$  and normalize images between 0 and 1. In LoFi-ADMM, we set  $\alpha = 0.05$  and execute it for 90 iterations, the hyper-parameters we found suitable to ensure convergence. Now, we run LoFi-ADMM to solve the image-inpainting problem at a higher resolution  $512 \times 512$  where  $p = 30\%$  of the image pixels are randomly masked. Figure 9 showcases the performance of the LoFi-ADMM on both in-distribution and OOD data. This experiment shows that once LoFi denoiser is trained, it can be used for solving general inverse problems at any higher resolution with a strong generalization.

**Radio interferometry.** We next apply LoFi-ADMM to radio interferometric imaging, please refer to Section S-I-F in the supplementary material for further information regarding the forward model. We use non-uniform fast Fourier transform (NUFFT) to simulate radio interferometric measurements from  $128 \times 128$  images using an upsampling factor of 2 and Kaiser-Bessel kernels with a size of  $6 \times 6$  pixels; we

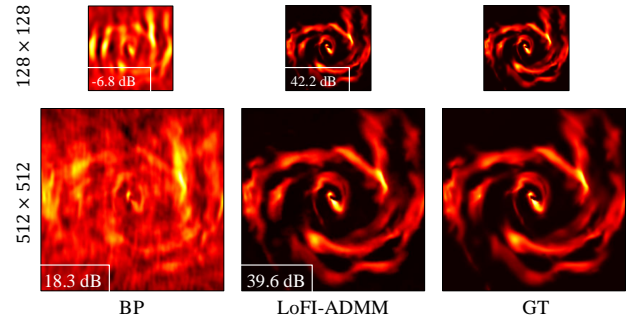


Fig. 10: LoFi-ADMM performance on radio interferometry; the LoFi prior is trained on low-resolution images  $128 \times 128$ .

use the simulated uv-coverage of the MeerKAT telescope and the measurements with complex Gaussian noise at the SNR of 30dB. We train LoFi denoiser on 13000 images of simulated galaxies created from the IllustrisTNG simulations [Nelson et al., 2019]. Figure 10 illustrates the performance of the LoFi-ADMM at original and higher resolutions. This experiment shows that LoFi-ADMM can conveniently exploit the measurements obtained from higher-resolution images for more accurate reconstructions with more details.

## VI. LIMITATIONS AND CONCLUSION

We introduced LoFi, a scalable local image reconstruction framework that stands out for its strong generalization on OOD data and resolution agnostic memory usage during training. Notably, our approach achieves strong performance on local inverse problems such as LDCT and image denoising, all while maintaining a significantly smaller memory footprint compared to standard CNNs. The strong inductive bias of LoFi allows us to conveniently train it on tiny datasets with few training samples without overfitting or needing regularization like early stopping. Our experiments demonstrate the effectiveness of LoFi as a denoising prior within the PnP framework, showcasing its ability to reconstruct images in arbitrary resolutions for tasks such as image in-painting and radio interferometric imaging.

Although LoFi’s pixel-based pipeline significantly reduces memory requirements—particularly during training, thus enabling high-dimensional reconstructions on smaller GPUs—it comes with trade-offs. Like INRs, the computational cost of LoFi in inference increases quadratically with image resolution.

Recent studies [He and Jin, 2023, 2024] have proposed strategies to enhance the efficiency of continuous image representation in INRs by increasing shared computations across pixels, thereby reducing computational complexity. Implementing similar strategies in LoFi could potentially reduce computations during inference, which we leave as a direction for future work.

## REFERENCES

- H. K. Aggarwal, M. P. Mani, and M. Jacob. Modl: Model-based deep learning architecture for inverse problems. *IEEE transactions on medical imaging*, 38(2):394–405, 2018.
- R. Ahmad, C. A. Bouman, G. T. Buzzard, S. Chan, S. Liu, E. T. Reehorst, and P. Schniter. Plug-and-play methods for magnetic resonance imaging: Using denoisers for image recovery. *IEEE signal processing magazine*, 37(1):105–116, 2020.
- F. Altekrüger, A. Denker, P. Hagemann, J. Hertrich, P. Maass, and G. Steidl. Patchnr: Learning from small data by patch normalizing flow regularization. *arXiv preprint arXiv:2205.12021*, 2022.
- M. Asim, M. Daniels, O. Leong, A. Ahmed, and P. Hand. Invertible generative models for inverse problems: mitigating representation error and dataset bias. In *International Conference on Machine Learning*, pages 399–409. PMLR, 2020.
- M. Atzmon and Y. Lipman. Sal: Sign agnostic learning of shapes from raw data. In *Proceedings of the IEEE/CVF conference on computer vision and pattern recognition*, pages 2565–2574, 2020.
- R. E. Blahut. *Theory of remote image formation*. Cambridge University Press, 2004.
- A. Bora, A. Jalal, E. Price, and A. G. Dimakis. Compressed sensing using generative models. In *International conference on machine learning*, pages 537–546. PMLR, 2017.
- S. Boyd, N. Parikh, E. Chu, B. Peleato, J. Eckstein, et al. Distributed optimization and statistical learning via the alternating direction method of multipliers. *Foundations and Trends® in Machine Learning*, 3(1):1–122, 2011.
- D. J. Brenner and E. J. Hall. Computed tomography—an increasing source of radiation exposure. *New England journal of medicine*, 357(22):2277–2284, 2007.
- M. M. Bronstein, J. Bruna, T. Cohen, and P. Veličković. Geometric deep learning: Grids, groups, graphs, geodesics, and gauges. *arXiv preprint arXiv:2104.13478*, 2021.
- A. Buades, B. Coll, and J.-M. Morel. A non-local algorithm for image denoising. In *2005 IEEE computer society conference on computer vision and pattern recognition (CVPR’05)*, volume 2, pages 60–65. Ieee, 2005.
- H. C. Burger, C. J. Schuler, and S. Harmeling. Image denoising: Can plain neural networks compete with bm3d? In *2012 IEEE conference on computer vision and pattern recognition*, pages 2392–2399. IEEE, 2012.
- R. Chabra, J. E. Lenssen, E. Ilg, T. Schmidt, J. Straub, S. Lovegrove, and R. Newcombe. Deep local shapes: Learning local sdf priors for detailed 3d reconstruction. In *Computer Vision—ECCV 2020: 16th European Conference, Glasgow, UK, August 23–28, 2020, Proceedings, Part XXIX 16*, pages 608–625. Springer, 2020.
- A. Chaman and I. Dokmanić. Truly shift-invariant convolutional neural networks. In *Proceedings of the IEEE/CVF Conference on Computer Vision and Pattern Recognition*, pages 3773–3783, 2021a.
- A. Chaman and I. Dokmanić. Truly shift-equivariant convolutional neural networks with adaptive polyphase upsampling. In *2021 55th Asilomar Conference on Signals, Systems, and Computers*, pages 1113–1120. IEEE, 2021b.
- S. H. Chan, X. Wang, and O. A. Elgandy. Plug-and-play adm for image restoration: Fixed-point convergence and applications. *IEEE Transactions on Computational Imaging*, 3(1):84–98, 2016.
- H. Chen, Y. Wang, T. Guo, C. Xu, Y. Deng, Z. Liu, S. Ma, C. Xu, C. Xu, and W. Gao. Pre-trained image processing transformer. In *Proceedings of the IEEE/CVF conference on computer vision and pattern recognition*, pages 12299–12310, 2021a.
- Y. Chen, S. Liu, and X. Wang. Learning continuous image representation with local implicit image function. In *Proceedings of the IEEE/CVF conference on computer vision and pattern recognition*, pages 8628–8638, 2021b.
- Z. Chen and H. Zhang. Learning implicit fields for generative shape modeling. In *Proceedings of the IEEE/CVF conference on computer vision and pattern recognition*, pages 5939–5948, 2019.
- H. Chung, J. Kim, M. T. Mccann, M. L. Klasky, and J. C. Ye. Diffusion posterior sampling for general noisy inverse problems. *arXiv preprint arXiv:2209.14687*, 2022.
- T. Cohen and M. Welling. Group equivariant convolutional networks. In *International conference on machine learning*, pages 2990–2999. PMLR, 2016a.
- T. S. Cohen and M. Welling. Steerable cnns. *arXiv preprint arXiv:1612.08498*, 2016b.
- K. Dabov, A. Foi, V. Katkovnik, and K. Egiazarian. Image denoising by sparse 3-d transform-domain collaborative filtering. *IEEE Transactions on image processing*, 16(8):2080–2095, 2007.
- J. Dai, H. Qi, Y. Xiong, Y. Li, G. Zhang, H. Hu, and Y. Wei. Deformable convolutional networks. In *Proceedings of the IEEE international conference on computer vision*, pages 764–773, 2017.
- N. Davoudi, X. L. Deán-Ben, and D. Razansky. Deep learning optoacoustic tomography with sparse data. *Nature Machine Intelligence*, 1(10):453–460, 2019.
- P. Dhariwal and A. Nichol. Diffusion models beat gans on image synthesis. *Advances in neural information processing systems*, 34:8780–8794, 2021.
- Z. Ding, M. Zhang, J. Wu, and Z. Tu. Patched denoising diffusion models for high-resolution image synthesis. In *The Twelfth International Conference on Learning Representations*, 2024.
- M. Diwakar and M. Kumar. A review on ct image noise and its denoising. *Biomedical Signal Processing and Control*, 42:73–88, 2018. ISSN 1746-8094. doi: <https://doi.org/10.1016/j.bspc.2018.01.010>.
- W. Dong, P. Wang, W. Yin, G. Shi, F. Wu, and X. Lu. Denoising

- prior driven deep neural network for image restoration. *IEEE transactions on pattern analysis and machine intelligence*, 41(10):2305–2318, 2018.
- A. Dosovitskiy, L. Beyer, A. Kolesnikov, D. Weissenborn, X. Zhai, T. Unterthiner, M. Dehghani, M. Minderer, G. Heigold, S. Gelly, et al. An image is worth 16x16 words: Transformers for image recognition at scale. *arXiv preprint arXiv:2010.11929*, 2020.
- E. Dupont, Y. W. Teh, and A. Doucet. Generative models as distributions of functions. *arXiv preprint arXiv:2102.04776*, 2021.
- E. Dupont, H. Kim, S. Eslami, D. Rezende, and D. Rosenbaum. From data to functa: Your data point is a function and you can treat it like one. *arXiv preprint arXiv:2201.12204*, 2022.
- Z. Fabian, B. Tinaz, and M. Soltanolkotabi. Humus-net: Hybrid unrolled multi-scale network architecture for accelerated mri reconstruction. *Advances in Neural Information Processing Systems*, 35:25306–25319, 2022.
- D. Gilton, G. Ongie, and R. Willett. Learned patch-based regularization for inverse problems in imaging. In *2019 IEEE 8th international workshop on computational advances in multi-sensor adaptive processing (campsap)*, pages 211–215. IEEE, 2019.
- K. He, X. Zhang, S. Ren, and J. Sun. Deep residual learning for image recognition. In *Proceedings of the IEEE conference on computer vision and pattern recognition*, pages 770–778, 2016.
- Z. He and Z. Jin. Dynamic implicit image function for efficient arbitrary-scale image representation. *arXiv preprint arXiv:2306.12321*, 2023.
- Z. He and Z. Jin. Latent modulated function for computational optimal continuous image representation. In *Proceedings of the IEEE/CVF Conference on Computer Vision and Pattern Recognition*, pages 26026–26035, 2024.
- B. Heo, S. Yun, D. Han, S. Chun, J. Choe, and S. J. Oh. Rethinking spatial dimensions of vision transformers. In *Proceedings of the IEEE/CVF international conference on computer vision*, pages 11936–11945, 2021.
- J. Hertrich, A. Houdard, and C. Redenbach. Wasserstein patch prior for image superresolution. *IEEE Transactions on Computational Imaging*, 8:693–704, 2022.
- J. Ho, A. Jain, and P. Abbeel. Denoising diffusion probabilistic models. *Advances in neural information processing systems*, 33:6840–6851, 2020.
- M. Holler, M. Guizar-Sicairos, E. H. Tsai, R. Dinapoli, E. Müller, O. Bunk, J. Raabe, and G. Aeppli. High-resolution non-destructive three-dimensional imaging of integrated circuits. *Nature*, 543(7645):402–406, 2017.
- M. Hssayeni, M. Croock, A. Salman, H. Al-khafaji, Z. Yahya, and B. Ghoraani. Computed tomography images for intracranial hemorrhage detection and segmentation. *Intracranial hemorrhage segmentation using a deep convolutional model. Data*, 5(1):14, 2020.
- C. M. Hyun, H. P. Kim, S. M. Lee, S. Lee, and J. K. Seo. Deep learning for undersampled mri reconstruction. *Physics in Medicine & Biology*, 63(13):135007, 2018.
- A. Jalal, M. Arvinte, G. Daras, E. Price, A. G. Dimakis, and J. Tamir. Robust compressed sensing mri with deep generative priors. *Advances in Neural Information Processing Systems*, 34:14938–14954, 2021.
- F. Jia, W. H. Wong, and T. Zeng. Ddunet: Dense dense u-net with applications in image denoising. In *Proceedings of the IEEE/CVF international conference on computer vision*, pages 354–364, 2021.
- C. Jiang, A. Sud, A. Makadia, J. Huang, M. Nießner, T. Funkhouser, et al. Local implicit grid representations for 3d scenes. In *Proceedings of the IEEE/CVF Conference on Computer Vision and Pattern Recognition*, pages 6001–6010, 2020.
- K. H. Jin, M. T. McCann, E. Froustey, and M. Unser. Deep convolutional neural network for inverse problems in imaging. *IEEE transactions on image processing*, 26(9):4509–4522, 2017.
- N. Kaiser and G. Squires. Mapping the Dark Matter with Weak Gravitational Lensing. *ApJ*, 404:441, Feb. 1993. doi: 10.1086/172297.
- U. S. Kamilov, C. A. Bouman, G. T. Buzzard, and B. Wohlberg. Plug-and-play methods for integrating physical and learned models in computational imaging: Theory, algorithms, and applications. *IEEE Signal Processing Magazine*, 40(1):85–97, 2023.
- T. Karras, T. Aila, S. Laine, and J. Lehtinen. Progressive growing of gans for improved quality, stability, and variation. *arXiv preprint arXiv:1710.10196*, 2017.
- B. Kawar, M. Elad, S. Ermon, and J. Song. Denoising diffusion restoration models. *Advances in Neural Information Processing Systems*, 35:23593–23606, 2022.
- A. Khorashadizadeh, A. Chaman, V. Debarnot, and I. Dokmanić. Funknn: Neural interpolation for functional generation. *ICLR*, 2023a.
- A. Khorashadizadeh, V. Khorashadizadeh, S. Eskandari, G. A. Vandenbosch, and I. Dokmanić. Deep injective prior for inverse scattering. *IEEE Transactions on Antennas and Propagation*, 2023b.
- A. Khorashadizadeh, K. Kothari, L. Salsi, A. A. Harandi, M. de Hoop, and I. Dokmanić. Conditional injective flows for bayesian imaging. *IEEE Transactions on Computational Imaging*, 9:224–237, 2023c.
- D. P. Kingma and J. Ba. Adam: A method for stochastic optimization. *arXiv preprint arXiv:1412.6980*, 2014.
- D. P. Kingma and P. Dhariwal. Glow: Generative flow with invertible 1x1 convolutions. *Advances in neural information processing systems*, 31, 2018.
- K. Kothari, M. de Hoop, and I. Dokmanić. Learning the geometry of wave-based imaging. *Advances in Neural Information Processing Systems*, 33:8318–8329, 2020.
- K. Kothari, A. Khorashadizadeh, M. de Hoop, and I. Dokmanić. Trumpets: Injective flows for inference and inverse problems. In *Uncertainty in Artificial Intelligence*, pages 1269–1278. PMLR, 2021.
- J. Leuschner, M. Schmidt, D. O. Bagger, and P. Maass. Lodopab-ct, a benchmark dataset for low-dose computed tomography reconstruction. *Scientific Data*, 8(1):109, 2021.
- A. Levin and B. Nadler. Natural image denoising: Optimality and inherent bounds. In *CVPR 2011*, pages 2833–2840. IEEE, 2011.

- J. Liang, J. Cao, G. Sun, K. Zhang, L. Van Gool, and R. Timofte. Swinir: Image restoration using swin transformer. In *Proceedings of the IEEE/CVF international conference on computer vision*, pages 1833–1844, 2021.
- T. I. Liaudat, M. Mars, M. A. Price, M. Pereyra, M. M. Betcke, and J. D. McEwen. Scalable Bayesian uncertainty quantification with data-driven priors for radio interferometric imaging. *arXiv e-prints*, art. arXiv:2312.00125, Nov. 2023. doi: 10.48550/arXiv.2312.00125.
- P. Liu, H. Zhang, K. Zhang, L. Lin, and W. Zuo. Multi-level wavelet-cnn for image restoration. In *Proceedings of the IEEE conference on computer vision and pattern recognition workshops*, pages 773–782, 2018.
- T. Liu, A. Chaman, D. Belius, and I. Dokmanić. Learning multiscale convolutional dictionaries for image reconstruction. *IEEE Transactions on Computational Imaging*, 8:425–437, 2022.
- T. Liu, T. Yang, Q. Zhang, and Q. Lei. Optimization for amortized inverse problems. In *International Conference on Machine Learning*, pages 22289–22319. PMLR, 2023.
- D. G. Lowe. Object recognition from local scale-invariant features. In *Proceedings of the seventh IEEE international conference on computer vision*, volume 2, pages 1150–1157. Ieee, 1999.
- R. Mandelbaum. Weak lensing for precision cosmology. *Annual Review of Astronomy and Astrophysics*, 56(1):393–433, 2018. doi: 10.1146/annurev-astro-081817-051928.
- Y. Mansour, K. Lin, and R. Heckel. Image-to-image mlp-mixer for image reconstruction. *arXiv preprint arXiv:2202.02018*, 2022.
- F. Marinacci, M. Vogelsberger, R. Pakmor, P. Torrey, V. Springel, L. Hernquist, D. Nelson, R. Weinberger, A. Pillepich, J. Naiman, and S. Genel. First results from the IllustrisTNG simulations: radio haloes and magnetic fields. *Monthly Notices of the Royal Astronomical Society*, 480(4): 5113–5139, Nov. 2018. doi: 10.1093/mnras/sty2206.
- M. T. McCann, K. H. Jin, and M. Unser. Convolutional neural networks for inverse problems in imaging: A review. *IEEE Signal Processing Magazine*, 34(6):85–95, 2017.
- B. Mildenhall, P. P. Srinivasan, M. Tancik, J. T. Barron, R. Ramamoorthi, and R. Ng. Nerf: Representing scenes as neural radiance fields for view synthesis. *Communications of the ACM*, 65(1):99–106, 2021.
- J. P. Naiman, A. Pillepich, V. Springel, E. Ramirez-Ruiz, P. Torrey, M. Vogelsberger, R. Pakmor, D. Nelson, F. Marinacci, L. Hernquist, R. Weinberger, and S. Genel. First results from the IllustrisTNG simulations: a tale of two elements - chemical evolution of magnesium and europium. *Monthly Notices of the Royal Astronomical Society*, 477(1):1206–1224, June 2018. doi: 10.1093/mnras/sty618.
- D. Nelson, A. Pillepich, V. Springel, R. Weinberger, L. Hernquist, R. Pakmor, S. Genel, P. Torrey, M. Vogelsberger, G. Kauffmann, F. Marinacci, and J. Naiman. First results from the IllustrisTNG simulations: the galaxy colour bimodality. *Monthly Notices of the Royal Astronomical Society*, 475(1):624–647, Mar. 2018. doi: 10.1093/mnras/stx3040.
- D. Nelson, A. Pillepich, V. Springel, R. Pakmor, R. Weinberger, S. Genel, P. Torrey, M. Vogelsberger, F. Marinacci, and L. Hernquist. First results from the tng50 simulation: galactic outflows driven by supernovae and black hole feedback. *Monthly Notices of the Royal Astronomical Society*, 490(3): 3234–3261, 2019.
- K. Osato, J. Liu, and Z. Haiman.  $\kappa$ TNG: effect of baryonic processes on weak lensing with IllustrisTNG simulations. *Monthly Notices of the Royal Astronomical Society*, 502(4): 5593–5602, 02 2021. ISSN 0035-8711. doi: 10.1093/mnras/stab395.
- S. Osher, M. Burger, D. Goldfarb, J. Xu, and W. Yin. An iterative regularization method for total variation-based image restoration. *Multiscale Modeling & Simulation*, 4(2):460–489, 2005.
- B. Park, S. Yu, and J. Jeong. Densely connected hierarchical network for image denoising. In *Proceedings of the IEEE/CVF conference on computer vision and pattern recognition workshops*, pages 0–0, 2019.
- S. Peng, M. Niemeyer, L. Mescheder, M. Pollefeys, and A. Geiger. Convolutional occupancy networks. In *Computer Vision—ECCV 2020: 16th European Conference, Glasgow, UK, August 23–28, 2020, Proceedings, Part III 16*, pages 523–540. Springer, 2020.
- A. Pillepich, D. Nelson, L. Hernquist, V. Springel, R. Pakmor, P. Torrey, R. Weinberger, S. Genel, J. P. Naiman, F. Marinacci, and M. Vogelsberger. First results from the IllustrisTNG simulations: the stellar mass content of groups and clusters of galaxies. *Monthly Notices of the Royal Astronomical Society*, 475(1):648–675, Mar. 2018. doi: 10.1093/mnras/stx3112.
- L. Pratley, J. D. McEwen, M. d’Avezac, R. E. Carrillo, A. Onose, and Y. Wiaux. Robust sparse image reconstruction of radio interferometric observations with purify. *Monthly Notices of the Royal Astronomical Society*, 473(1):1038–1058, 09 2017. ISSN 0035-8711. doi: 10.1093/mnras/stx2237.
- M. A. Price, J. D. McEwen, L. Pratley, and T. D. Kitching. Sparse Bayesian mass-mapping with uncertainties: Full sky observations on the celestial sphere. *Monthly Notices of the Royal Astronomical Society*, 500(4):5436–5452, 11 2020. ISSN 0035-8711. doi: 10.1093/mnras/staa3563.
- O. Puny, M. Atzmon, H. Ben-Hamu, I. Misra, A. Grover, E. J. Smith, and Y. Lipman. Frame averaging for invariant and equivariant network design. *arXiv preprint arXiv:2110.03336*, 2021.
- Y. Romano, M. Elad, and P. Milanfar. The little engine that could: Regularization by denoising (red). *SIAM Journal on Imaging Sciences*, 10(4):1804–1844, 2017.
- O. Ronneberger, P. Fischer, and T. Brox. U-net: Convolutional networks for biomedical image segmentation. In *Medical Image Computing and Computer-Assisted Intervention—MICCAI 2015: 18th International Conference, Munich, Germany, October 5–9, 2015, Proceedings, Part III 18*, pages 234–241. Springer, 2015.
- A. Sannai, M. Kawano, and W. Kumagai. Equivariant and invariant reynolds networks. *arXiv preprint arXiv:2110.08092*, 2021.
- V. Sitzmann, J. Martel, A. Bergman, D. Lindell, and G. Wetzstein. Implicit neural representations with periodic activation functions. *Advances in neural information processing*

- systems*, 33:7462–7473, 2020.
- V. Springel, R. Pakmor, A. Pillepich, R. Weinberger, D. Nelson, L. Hernquist, M. Vogelsberger, S. Genel, P. Torrey, F. Marinacci, and J. Naiman. First results from the IllustrisTNG simulations: matter and galaxy clustering. *Monthly Notices of the Royal Astronomical Society*, 475(1):676–698, Mar. 2018. doi: 10.1093/mnras/stx3304.
- A. R. Thompson, J. M. Moran, and J. Swenson, George W. *Interferometry and Synthesis in Radio Astronomy, 3rd Edition*. 2017. doi: 10.1007/978-3-319-44431-4.
- I. O. Tolstikhin, N. Houlsby, A. Kolesnikov, L. Beyer, X. Zhai, T. Unterthiner, J. Yung, A. Steiner, D. Keysers, J. Uszkoreit, et al. Mlp-mixer: An all-mlp architecture for vision. *Advances in neural information processing systems*, 34: 24261–24272, 2021.
- A. Trockman and J. Z. Kolter. Patches are all you need? *arXiv preprint arXiv:2201.09792*, 2022.
- B. S. Veeling, J. Linmans, J. Winkens, T. Cohen, and M. Welling. Rotation equivariant cnns for digital pathology. In *Medical Image Computing and Computer Assisted Intervention—MICCAI 2018: 21st International Conference, Granada, Spain, September 16-20, 2018, Proceedings, Part II 11*, pages 210–218. Springer, 2018.
- S. V. Venkatakrisnan, C. A. Bouman, and B. Wohlberg. Plug-and-play priors for model based reconstruction. In *2013 IEEE global conference on signal and information processing*, pages 945–948. IEEE, 2013.
- T. Vlašić, H. Nguyen, A. Khorashadizadeh, and I. Dokmanić. Implicit neural representation for mesh-free inverse obstacle scattering. In *2022 56th Asilomar Conference on Signals, Systems, and Computers*, pages 947–952. IEEE, 2022.
- G. Wang, H. Yu, and B. De Man. An outlook on x-ray ct research and development. *Medical physics*, 35(3):1051–1064, 2008.
- W. Wang, E. Xie, X. Li, D.-P. Fan, K. Song, D. Liang, T. Lu, P. Luo, and L. Shao. Pyramid vision transformer: A versatile backbone for dense prediction without convolutions. In *Proceedings of the IEEE/CVF international conference on computer vision*, pages 568–578, 2021.
- Z. Wang, A. C. Bovik, H. R. Sheikh, and E. P. Simoncelli. Image quality assessment: from error visibility to structural similarity. *IEEE transactions on image processing*, 13(4): 600–612, 2004.
- Z. Wang, X. Cun, J. Bao, W. Zhou, J. Liu, and H. Li. Uformer: A general u-shaped transformer for image restoration. In *Proceedings of the IEEE/CVF conference on computer vision and pattern recognition*, pages 17683–17693, 2022.
- Z. Wang, Y. Jiang, H. Zheng, P. Wang, P. He, Z. Wang, W. Chen, M. Zhou, et al. Patch diffusion: Faster and more data-efficient training of diffusion models. *Advances in Neural Information Processing Systems*, 36, 2024.
- K. Wei, A. Aviles-Rivero, J. Liang, Y. Fu, C.-B. Schönlieb, and H. Huang. Tuning-free plug-and-play proximal algorithm for inverse imaging problems. In *International Conference on Machine Learning*, pages 10158–10169. PMLR, 2020.
- K. Wei, A. Aviles-Rivero, J. Liang, Y. Fu, H. Huang, and C.-B. Schönlieb. Tfpnp: Tuning-free plug-and-play proximal algorithms with applications to inverse imaging problems. *The Journal of Machine Learning Research*, 23(1):699–746, 2022.
- Z. Wei and X. Chen. Deep-learning schemes for full-wave nonlinear inverse scattering problems. *IEEE Transactions on Geoscience and Remote Sensing*, 57(4):1849–1860, 2018.
- F. Yu, A. Seff, Y. Zhang, S. Song, T. Funkhouser, and J. Xiao. Lsun: Construction of a large-scale image dataset using deep learning with humans in the loop. *arXiv preprint arXiv:1506.03365*, 2015.
- S. W. Zamir, A. Arora, S. Khan, M. Hayat, F. S. Khan, and M.-H. Yang. Restormer: Efficient transformer for high-resolution image restoration. In *Proceedings of the IEEE/CVF conference on computer vision and pattern recognition*, pages 5728–5739, 2022.
- K. Zhang, W. Zuo, Y. Chen, D. Meng, and L. Zhang. Beyond a gaussian denoiser: Residual learning of deep cnn for image denoising. *IEEE transactions on image processing*, 26(7): 3142–3155, 2017a.
- K. Zhang, W. Zuo, S. Gu, and L. Zhang. Learning deep cnn denoiser prior for image restoration. In *Proceedings of the IEEE conference on computer vision and pattern recognition*, pages 3929–3938, 2017b.
- K. Zhang, Y. Li, W. Zuo, L. Zhang, L. Van Gool, and R. Timofte. Plug-and-play image restoration with deep denoiser prior. *IEEE Transactions on Pattern Analysis and Machine Intelligence*, 44(10):6360–6376, 2021.
- Z. Zhao and A. Singer. Rotationally invariant image representation for viewing direction classification in cryo-em. *Journal of structural biology*, 186(1):153–166, 2014.
- Y. Zhu, K. Zhang, J. Liang, J. Cao, B. Wen, R. Timofte, and L. Van Gool. Denoising diffusion models for plug-and-play image restoration. In *Proceedings of the IEEE/CVF Conference on Computer Vision and Pattern Recognition*, pages 1219–1229, 2023.
- D. Zoran and Y. Weiss. From learning models of natural image patches to whole image restoration. In *2011 international conference on computer vision*, pages 479–486. IEEE, 2011.

## Supplementary Materials

### S-I. NETWORK ARCHITECTURE AND TRAINING DETAILS

We describe the network architecture and training details of LoFi and CNN baselines used in the experiments in Section V.

#### A. Low-dose computed tomography

For this experiment, we parameterize LoFi with multiMLP architecture depicted in Figure 2 where we used 9 MLP modules, each with three hidden layers of dimension 370 with ReLu activations and the output layer has 100 neurons. Their outputs are then concatenated and mixed by another MLP with an input layer of size  $900 = 9 \times 100$  and 3 hidden layers of dimension 370 with ReLu activations. We consider  $K = 81$  neighboring pixels initialized with circular geometry, 9 circles each with 9 points uniformly distributed around the centric coordinate. Regarding the pre-processing filter, we concatenated the real and complex values of the filtered input image along the channel dimension before patch extraction. Regarding the architecture of baselines, we used the standard implementations published by the authors with the following configurations.

**DnCNN:** number of layers=15, number of channels=160

**IRCNN:** number of layers = 13, number of channels = 256

**U-Net:** Init-features = 32

**DRU-Net:** Init-features = 32

#### B. Image denoising

Similar to the experiment for LDCT, we used multiMLP architecture with the same structure. For this particular experiment, we did not use the pre-processing filter to avoid overfitting as our training set is very small. Regarding the architecture of baselines, we used smaller networks for U-Net and DRU-Net for having a fair comparison with other baselines and LoFi in terms of overfitting.

**U-Net:** Init-features = 19

**DRU-Net:** Init-features = 19

With these parameters, all baselines and LoFi have approximately 3M parameters.

#### C. Dark matter mapping

For this experiment, we used the same network architecture as the experiment of LDCT for both LoFi and baselines. Regarding dark matter mapping simulations, we used the  $\kappa$ TNG convergence maps [Osato et al., 2021], generated from the widely used IllustrisTNG hydrodynamical simulation suite [Pillepich et al., 2018, Springel et al., 2018, Naiman et al., 2018, Nelson et al., 2018, Marinacci et al., 2018], to build the train and test datasets for the models presented in Figure 6. The  $\kappa$ TNG dataset consists of 10 000 realizations of  $5 \times 5 \text{deg}^2$  convergence maps for each of the 40 different source redshifts with  $0 < z_s < 2.6$ . For the sake of simplicity, we have selected a single redshift slice, the 20<sup>th</sup> plane, corresponding to  $z_s = 0.858$  for our experiments.

From the simulated convergence fields,  $\kappa$ , we have constructed the observed shear fields using Equation 5. We

follow [Price et al., 2020, §5.2.1] for the noise simulation. The shear noise  $\mathbf{n}$  for each component of the shear and for each pixel  $i$  is simulated as  $\mathbf{n}_i \sim \mathcal{N}(0, \sigma_i^2)$ . The per-pixel standard deviation can be computed as follows

$$\sigma_i = \frac{\sigma_e}{\sqrt{(\theta^2/n_{\text{grid}}^2) \times n_{\text{gal}}}}, \quad (\text{S1})$$

where  $\sigma_e$  is the standard deviation of the intrinsic ellipticity distribution,  $\theta^2$  is the area of the simulated field in  $\text{arcmin}^2$ ,  $n_{\text{grid}}^2$  is the total number of pixels in the field, and  $n_{\text{gal}}$  is the number density of galaxy observations given in number of galaxies per  $\text{arcmin}^2$ . We have used  $\sigma_e = 0.37$ , which is the typical intrinsic ellipticity standard deviation,  $\theta = 300$  arcmin, which corresponds to the  $\kappa$ TNG simulated area of  $5 \times 5 \text{deg}^2$ ,  $n_{\text{gal}} = 30 \text{ arcmin}^{-2}$ , which corresponds to the projected number density expected in Stage IV surveys like *Euclid*, and  $n_{\text{grid}} = 128$ .

#### D. Training details

LoFi is implemented in PyTorch on a machine with an Nvidia A100 GPU with 80GB memory. LoFi and baselines were trained for 200 epochs with  $\ell_1$  loss using Adam optimizer [Kingma and Ba, 2014] with learning rate  $10^{-4}$  and object batch size 64. In the case of LoFi, for each mini-batch of random objects, we performed optimization on a random mini-batch of 512 pixels 2 times.

#### E. Plug-and-Play ADMM

The PnP algorithm [Venkatakrisnan et al., 2013] is developed based on the alternating direction method of multipliers (ADMM) [Boyd et al., 2011], where new variables  $\mathbf{u}$  and  $\mathbf{v}$  are introduced to decouple the data fidelity and regularization terms in (1) as follows,

$$\min_{\mathbf{f}, \mathbf{v}} \max_{\mathbf{u}} \left\{ \frac{1}{2\sigma^2} \|\mathbf{q} - \mathbf{A}\mathbf{f}\|_2^2 + R(\mathbf{v}) + \frac{1}{2\eta} \|\mathbf{f} - \mathbf{v} + \mathbf{u}\|_2^2 - \frac{1}{2\eta} \|\mathbf{u}\|_2^2 \right\}, \quad (\text{S2})$$

where  $\eta$  is a penalty parameter that adjusts the convergence rate. We alternate the optimization on  $\mathbf{f}$ ,  $\mathbf{u}$  and  $\mathbf{v}$  as follows,

$$\mathbf{f}_k = h(\mathbf{v}_{k-1} - \mathbf{u}_{k-1}; \alpha), \quad (\text{S3})$$

$$\mathbf{v}_k = \text{prox}_R(\mathbf{f}_k - \mathbf{u}_{k-1}; \eta), \quad (\text{S4})$$

$$\mathbf{u}_k = \mathbf{u}_{k-1} + (\mathbf{f}_k - \mathbf{v}_k), \quad (\text{S5})$$

where  $\alpha = \frac{\sigma^2}{\eta}$  and,

$$h(\mathbf{z}; \alpha) \triangleq (\mathbf{A}^* \mathbf{A} + \alpha)^{-1} (\mathbf{A}^* \mathbf{q} + \alpha \mathbf{z}), \quad (\text{S6})$$

$$\text{prox}_R(\mathbf{z}; \eta) \triangleq \underset{\mathbf{f}}{\text{argmin}} \frac{1}{2\eta} \|\mathbf{f} - \mathbf{z}\|_2^2 + R(\mathbf{f}), \quad (\text{S7})$$

where  $\mathbf{A}^*$  is the adjoint forward operator. The proximal operator in (S7) can be interpreted as the denoiser of  $\mathbf{z}$  with image prior  $R(\cdot)$  and AWGN variance  $\eta$ . The key idea of the PnP algorithm is to employ a powerful image denoiser, like a pre-trained CNN, for (S7).

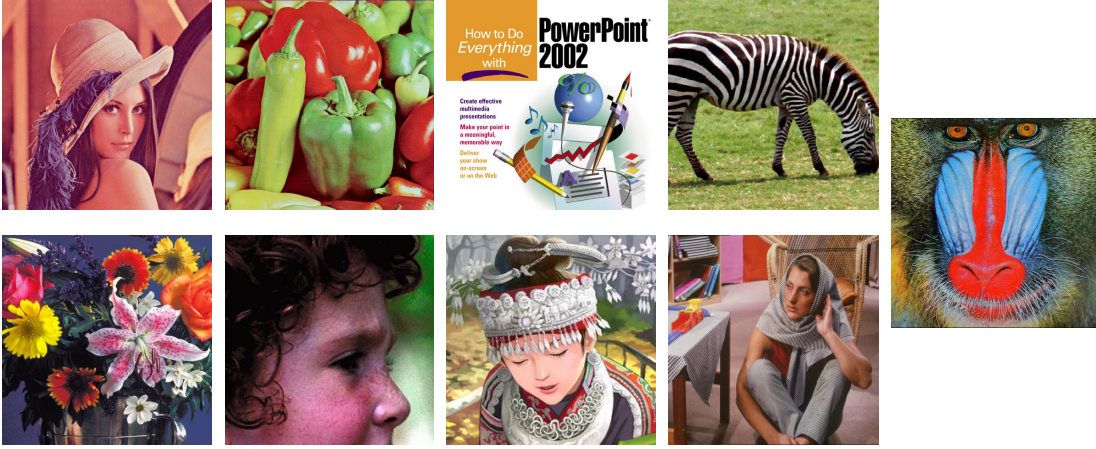


Fig. S1: Training dataset used for image denoising experiment in resolution  $512 \times 512$ .

### F. Radio interferometric imaging

Radio interferometry is an imaging technique where we acquire samples of the Fourier transform of the image along curves [Thompson et al., 2017, Pratley et al., 2017, Liaudat et al., 2023]. In radio interferometric imaging, aperture synthesis techniques are used to acquire specific Fourier measurements giving an incomplete coverage of the Fourier plane. The inverse problem consists of recovering the entire intensity image from Fourier measurements. In this case, the forward operator in a simplified form writes

$$\mathbf{A} = \mathbf{M}_{\text{RI}} \mathbf{F} \quad (\text{S8})$$

where  $\mathbf{M}_{\text{RI}}$  is a Fourier mask indicating the Fourier coverage of the observations. We have omitted gridding and degriding operations in between other corrections from the forward operator for the sake of simplicity; a more detailed description of the operator can be found in [Pratley et al., 2017, §3.2].

### S-II. FUTHER ANALYSIS AND ADDITIONAL EXPERIMENTS

In this section, we provide further analysis of LoFi architecture and additional experiments.

#### A. High-dimensional image denoising

Figure S2 illustrates the reconstructed images by LoFi on image denoising task ( $\sigma = 0.2$ ) in resolution  $1024 \times 1024$  which confirms the expressivity of the proposed framework even on very large images.

#### B. Equivariance to shifts and rotations

In many imaging and pattern recognition tasks, it is desirable to work with functions that are invariant or equivariant to shifts and rotations. Building such invariances into CNNs, typically via group representation theory [Cohen and Welling, 2016a, Bronstein et al., 2021] improves generalization both in and out of distribution [Cohen and Welling, 2016b, Veeling et al., 2018].

It is easy to see that LoFi is shift equivariant by design. Indeed, the patch at position  $\mathbf{x} + \Delta\mathbf{x}$  in an image shifted by

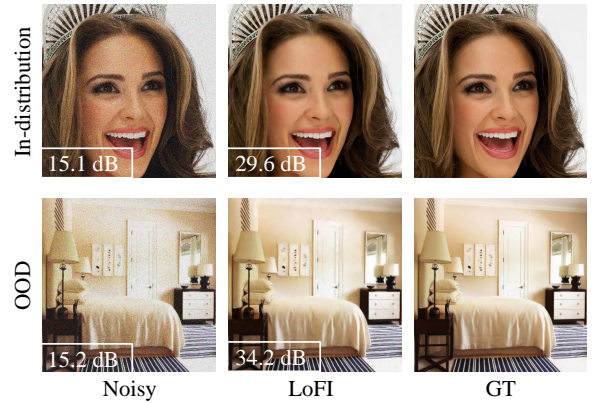


Fig. S2: LoFi reconstructions on in-distribution and OOD data for image denoising ( $\sigma = 0.2$ ) in resolution  $1024 \times 1024$ .

$\Delta\mathbf{x}$  is exactly the same as the patch at position  $\mathbf{x}$  in a non-shifted image; the  $\text{NN}_\theta$  (MultiMLP) thus receives the same input. This stands in contrast to most mainstream multi-scale CNNs which are surprisingly sensitive even to 1-pixel shifts, although equivariance can be restored by a careful design of pooling and downsampling layers [Chaman and Dokmanić, 2021b,a].

Rotation equivariance is precluded for square patches, except for angles that are multiples of  $\frac{\pi}{2}$ . With circular patches shown in Figure 2, when the image is rotated the  $\text{NN}_\theta$  receives the same input only in a different order up to interpolation error. Rotation equivariance could be implemented by applying  $\text{NN}_\theta$  to rotation invariant features [Lowe, 1999, Puny et al., 2021, Sannai et al., 2021, Zhao and Singer, 2014] extracted from the circular patch or by averaging the output over rotations. Even without this, however, LoFi is approximately rotation equivariant because natural images are approximately *locally* rotation invariant and the patch geometry is initialized as circular.

Now, we assess LoFi performance on the image denoising task when the input image is shifted or rotated. As shown in Figure S3, we horizontally shifted the input noisy image for 15 pixels. As expected, LoFi's reconstruction is shifted for 15 pixels and exhibits no degradation in the reconstruction quality.

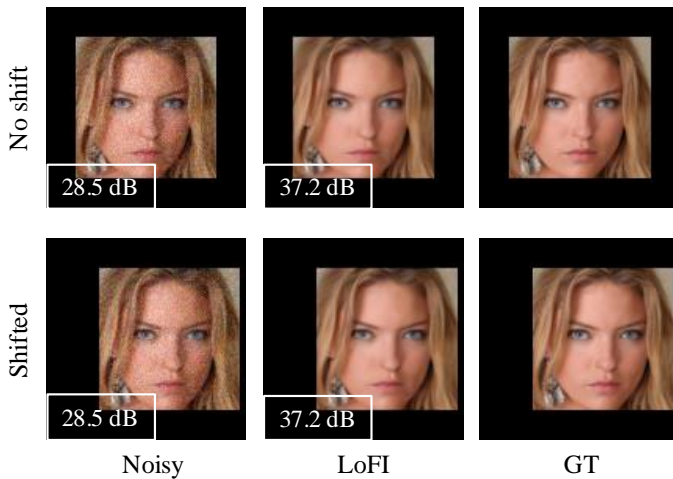


Fig. S3: Shift equivariance analysis for LoFi architecture; LoFi exhibits no degradation in reconstruction quality when the input noisy image is shifted for 15 pixels.



Fig. S4: Rotation equivariance analysis for LoFi architecture; LoFi exhibits minimal degradation in reconstruction quality when the input noisy image undergoes a 90-degree rotation.

This experiment confirms that LoFi is a truly shift equivariant network.

Figure S4 demonstrates the LoFi performance when the input noisy image undergoes a 90-degree rotation. As expected, we observe minimal degradation in reconstruction quality which shows LoFi’s strong robustness under rotation. Note that, we did not use any data augmentation to make the model robust under translation and rotation during training.

### C. Learned filter

In this section, we analyze the learned filter  $\mathbf{H}$  in (15) to understand how it processes noisy images. As shown in Figure S5, the learned filter remains local in data space after training which prevents  $\text{NN}_\theta$  from overfitting the large-scale features.

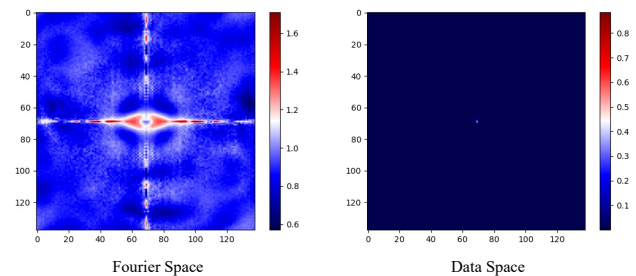


Fig. S5: The learned filter  $\mathbf{H}$  in (15); as expected, it has a small support in data space which prevents the  $\text{NN}_\theta$  from overfitting large-scale features.